metals

MDPI

Article

Effect of Milling Parameters on the Development of a Nanostructured FCC–TiNb15Mn Alloy via High-Energy Ball Milling

Cristina García-Garrido [1,*], Ranier Sepúlveda Ferrer [2], Christopher Salvo [3], Lucía García-Domínguez [2], Luis Pérez-Pozo [4], Pedro Javier Lloreda-Jurado [2] and Ernesto Chicardi [2,*]

[1] Instituto Andaluz del Patrimonio Histórico (IAPH), Camino de los Descubrimientos s/n, 41092 Sevilla, Spain
[2] Departamento de Ingeniería y Ciencia de los Materiales y del Transporte, Universidad de Sevilla, Av. Camino de los Descubrimientos s/n, 41092 Sevilla, Spain; rsepulveda@us.es (R.S.F.); lucgardom@alum.us.es (L.G.-D.); plloreda@us.es (P.J.L.-J.)
[3] Departamento de Ingeniería Mecánica, Facultad de Ingeniería, Universidad del Bío-Bío, Concepción 4081112, Chile; csalvo@ubiobio.cl
[4] Departamento de Ingeniería Mecánica, Universidad Técnica Federico Santamaría, Valparaíso 2340000, Chile; luis.perez@usm.cl
* Correspondence: cristina.g.garrido@juntadeandalucia.es (C.G.-G.); echicardi@us.es (E.C.)

Abstract: In this work, a blend of Ti, Nb, and Mn powders, with a nominal composition of 15 wt.% of Mn, and balanced Ti and Nb wt.%, was selected to be mechanically alloyed by the following two alternative high-energy milling devices: a vibratory 8000D mixer/mill® and a PM400 Retsch® planetary ball mill. Two ball-to-powder ratio (BPR) conditions (10:1 and 20:1) were applied, to study the evolution of the synthesized phases under each of the two mechanical alloying conditions. The main findings observed include the following: (1) the sequence conversion evolved from raw elements to a transitory bcc-TiNbMn alloy, and subsequently to an fcc-TiNb15Mn alloy, independent of the milling conditions; (2) the total full conversion to the fcc-TiNb15Mn alloy was only reached by the planetary mill at a minimum of 12 h of milling time, for either of the BPR employed; (3) the planetary mill produced a non-negligible Fe contamination from the milling media, when the highest BPR and milling time were applied; and (4) the final fcc-TiNb15Mn alloy synthesized presents a nanocrystalline nature and a partial degree of amorphization.

Keywords: Ti alloy; Nb; Mn; mechanical alloying; planetary mill; mixer mill

check for updates

Citation: García-Garrido, C.; Sepúlveda Ferrer, R.; Salvo, C.; García-Domínguez, L.; Pérez-Pozo, L.; Lloreda-Jurado, P.J.; Chicardi, E. Effect of Milling Parameters on the Development of a Nanostructured FCC–TiNb15Mn Alloy via High-Energy Ball Milling. *Metals* **2021**, *11*, 1225. https://doi.org/10.3390/met11081225

Academic Editors: Peng Cao and Tadeusz Kulik

Received: 16 June 2021
Accepted: 29 July 2021
Published: 31 July 2021

Publisher's Note: MDPI stays neutral with regard to jurisdictional claims in published maps and institutional affiliations.

Copyright: © 2021 by the authors. Licensee MDPI, Basel, Switzerland. This article is an open access article distributed under the terms and conditions of the Creative Commons Attribution (CC BY) license (https://creativecommons.org/licenses/by/4.0/).

1. Introduction

Titanium and its alloys are widely used for diverse applications, such as aerospace, architecture, medicine, chemical processing, power generation, marine and offshore sports equipment, and transportation [1]. Their low density, high mechanical strength, and high resistance to corrosion make them interesting for these fields [2]. In biomedical applications, the Ti6Al4V alloy is one of the most widely used metallic materials for bone-replacement implants, due to its excellent biocompatibility, high corrosion resistance to body fluids, and its good processability [3]. In the aerospace industry, Ti alloys are mainly used due to their excellent strength-to-weight ratio, excellent galvanic compatibility with polymer matrix composites, their stability at high temperatures, and their fatigue strength [4]. They are often employed in parts for turbine engine, airframe structures, wing boxes, bulkheads, and in numerous other aerospace applications.

However, certain properties of these Ti alloys must be modified to fit the application requirements. In particular, for bone implant applications, Ti and the Ti6Al4V alloy present the following several mechanical drawbacks that must be overcome: their higher level of stiffness (elastic modulus, E, greater than 100 GPa) in comparison with bone tissue (4–30 GPa, for trabecular and cortical bone, respectively) produces the undesirable

stress-shielding phenomenon (i.e., the incomplete load transference from implant to the bone) that can trigger bone resorption, thereby causing a loosening and/or premature failure of the implant. In turn, for aerospace applications, several of the main problems are associated with the high cost, the challenging machinability, the difficulties encountered in the cold forming, and the fluctuating product availability [5,6].

In this context, metastable beta Ti alloys, with a body-centered cubic structure (bcc), are studied as potential bone-replacement implant materials, due to their lower elastic modulus, and, therefore, to their ability to reduce the aforementioned stress-shielding phenomenon. The high-temperature Ti allotropic structure could be stabilized at room temperature by adding Betagen elements, such as Nb, Ta, Mo, V, Fe, and Cr, which lower the alpha–beta *transus* temperature [3,7]. Moreover, the beta Ti alloys have shown the highest strength of Ti alloys hitherto developed, typically with a yield strength greater than 1000 MPa [5].

In addition, Ti alloys with structures that are different to hcp and bcc, could be developed to increase the ductility for the enhancement of the machinability and the cold-forming process. To this end, and considering that the most plastically and isotropic deformable structure is the face-centered cubic (fcc) structure, due to its higher sliding system and symmetric structure, the development of new fcc Ti alloys, to improve their ductility, could prove interesting. In this way, Garcia-Garrido et al. [8,9] have already obtained fcc Ti alloys in the TiNbTa and TiNb (0–12 wt.%) Mn, thanks to the ability of Nb, Ta, and Mn to promote the formation of Ti-fcc, Ti-bcc, and Ti amorphous alloys, depending on the synthesis conditions [10–13]. In addition, Wu et al. [14] studied the formation of fcc-Ti from hcp-Ti by col-rolling (CR), and Hong et al. [15] by cryogenic channel die compression (CCDC). Thus, a severe plastic deformation (SPD) seems to be necessary to produce the fcc structure in Ti alloys, such as mechanical alloying (MA), CR, or CCDC, among others.

Concretely, the syntheses carried out by Garcia-Garrido et al. [8,9] were possible by means of MA, which has been reported to be a simple, economic, and reproducible method, in the following ways: to extend the metal solubility; to produce complete solid solutions; to refine the structure up to nanometric levels, and to synthesize new crystalline phases, such as the novel high-entropy alloys (HEAs) [16], quasi-crystalline phases, and amorphous phases, among other interesting abilities [17]. With respect to MA, it has been established that not only the rate of the reaction, but also the reaction route and the products obtained, can be highly influenced by using different milling equipment and milling conditions [18–20].

For these reasons, the present work is focused on the synthesis of a TiNb15Mn (in wt.%) alloy through MA, by employing two different devices (a PM 400 planetary ball mill, and an 8000D mixer/mill® shaker mill) and two different ball-to-powder ratios (10:1 and 20:1). The effects of these milling parameters and devices used on the crystallographic structure, and the morphology of this TiNb15Mn alloy, are subsequently investigated and discussed.

2. Materials and Methods

Powder blends of elemental titanium (CAS number 7440-32-6, 99.6% purity, <325 mesh, NOAH tech., San Antonio, TX, USA), niobium (CAS number 7440-03-1, 99.9% purity, <325 mesh, NOAH tech., San Antonio, TX, USA), and manganese powders (CAS number 7439-96-5, 99.9% purity, <325 mesh, NOAH tech., San Antonio, TX, USA), with a nominal composition of Ti0.55Nb0.28Mn0.17, corresponding to a 42.5 wt.% of Ti, 42.5 wt.% of Nb (i.e., balanced Ti–Nb weight percentage), and 15 wt.% of Mn, were mechanically alloyed in the following two different milling devices: a planetary ball mill (PM400, Retsch®, Haan, Germany) and an 8000D mixer/mill® high-energy ball mill (SPEX®, Sample Prep, New Jersey, NJ, USA). For the milling processes carried out in the PM400 planetary ball mill, ball-to-powder ratio (BPR) conditions of 10:1 and 20:1 were fixed with 95 balls (8 mm in diameter and 2.1 g in weight per ball) in a cylindrical-shaped vial (300 mL in volume). The

balls and vial used are composed of tempered stainless steel, and 20 g and 10 g of powder blend were introduced to modify the BPR to 10 and 20, respectively.

In turn, for the 8000D mixer/mill®, 5 g of the powder blend was milled with a BPR condition of 10:1, using the same type of balls (in this case, 24 balls) and vial (45 mL of volume) fabricated in tempered stainless steel. Mechanical alloying was carried out under an argon inert atmosphere ($H_2O \leq 8$ ppm and $O_2 \leq 2$ ppm, Linde Group, Spain) and at a spinning rate of 300 rpm for the PM400 planetary ball mill and at 50 Hz of frequency for the 8000D mixer/mill®. In addition, 2 wt.% of stearic acid (57-11-4 CAS number, 98% purity, Alfa-Aesar, Ward Hill, MA, USA) was added to the mixtures as a process control agent (PCA) to avoid excessive welding between the powder, balls, and vials. At 6, 8, 12, and 24 h of milling time, approximately 0.25 g of powder was extracted from the vials to study the phase evolution during mechanical alloying. A schema of the TiNb15Mn synthesis process is presented in Figure 1.

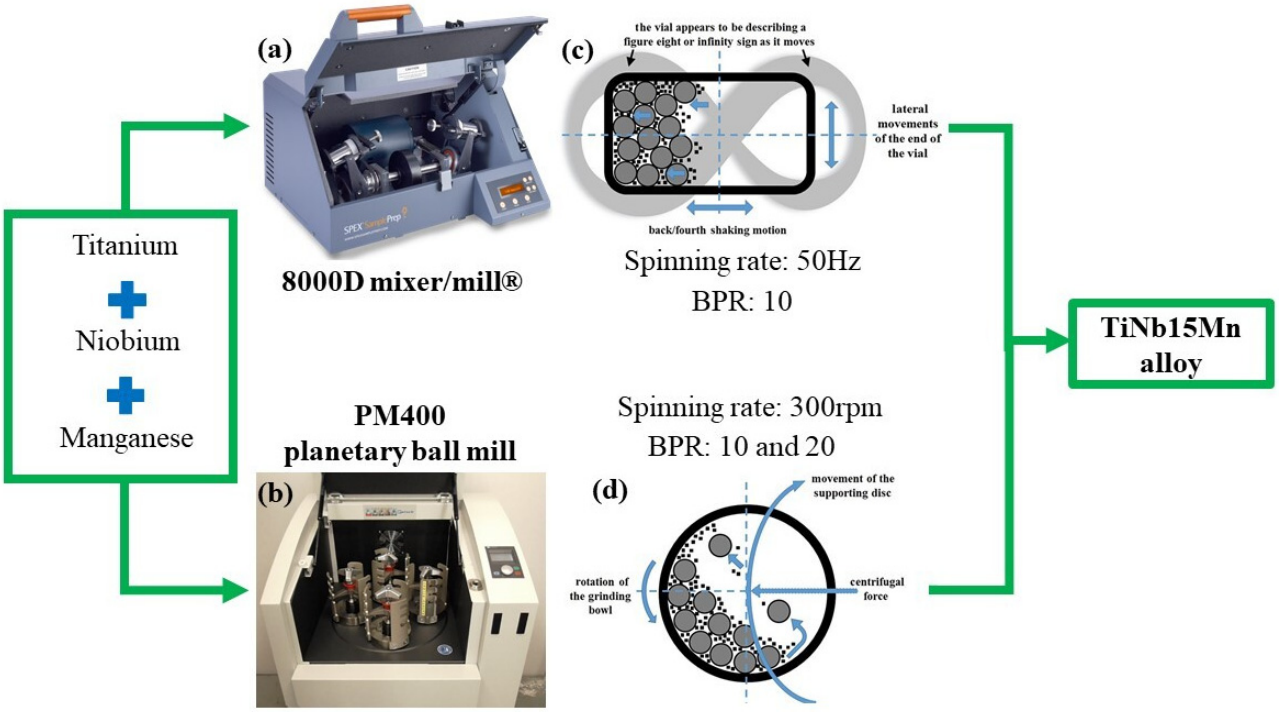

Figure 1. Schema of the mechanical alloying process carried out in both 8000D mixer/mill® and PM400 planetary ball mill for the TiNbMn system.

The as-milled powders were collected in an inert box (850-NB nitrogen dry box, Plas-Labs Inc., Lansing, MI, USA) under argon atmosphere and dispersed in acetone to prevent oxidation during handling. The as-milled powders obtained were labelled as PL for PM400 planetary ball mill, and as SP, from SPEX, for the 8000D mixer/mill®, following the BPR value (10 or 20) and the milling time (6, 12, 18 and 24 h). Therefore, the twelve as-milled powdered specimens were as follows: PL10_6h, PL10_12h, PL10_18h, PL10_24h, PL20_6h, PL20_12h, PL20_18h, PL20_24h, SP10_6h, SP10_12h, SP10_18h, and SP10_24h.

In order to characterize the phase evolution of the as-milled powders, X-ray diffraction (XRD) patterns were obtained using an X'Pert Pro instrument (PANalytical, Malvern, UK), equipped with a θ/θ goniometer, a Cu Kα radiation source (40 kV, 40 mA), a secondary Kb filter, a secondary diffracted beam monochromator to reduce the fluorescence, and an X'Celerator detector. The XRD patterns were collected by scanning from 2θ between 20° and 150° in the step-scan mode with 0.03° steps and a counting time of 5 s/step. Lanthanum hexaboride, LaB6 (Standard Reference Material 660b, NIST, Gaithersburg, MD, USA) was used to correct the instrumental error of the diffractometer and calibrate the positions of the diffraction peaks. The structural elucidations and the space group

symmetry (SGS) of phases formed were determined by the Dicvol software and compared by the Crystallography Open Database (COD). In order to deconvolute the peak overlapping at 2θ between 30° and 50°, a Rietveld refinement was carried out by applying the X'Pert HighScore Plus software (Malvern Panalytical B.V., Eindhoven, The Netherlands) using a pseudo-Voigt profile function [21]. All peaks for each diffractogram (including the deconvoluted peaks) were employed to obtain the lattice parameters *a* and the crystalline domain size D.

Scanning electron microscopy (SEM) images of the as-milled powders were obtained on a Hitachi S-4800 field emission scanning electron microscope (SEM) at 5 kV of acceleration voltage. For the Ti, Nb, Mn, and Fe (from the milling media) transition metals, and for the C and O, the atomic percentages were measured by X-ray energy-dispersive spectrometry (XEDS) using a detector coupled to the SEM at 30 kV of acceleration voltage. Twenty points were measured at each specimen to ensure statistical accuracy. Under the same experimental conditions, XEDS-SEM mappings were obtained. The particle morphology and average size (d) were obtained by image analysis (IA) from 5 SEM images taken at different magnifications (1 kX, 2 kX, and 5 kX) using the Image-Pro Plus® 6.2. software.

High-resolution transmission electron microscopy (HRTEM) and electron diffraction (ED) images were obtained for as-milled powder specimens on a TECNAI G2 F30 S-twin microscope (FEI Company, Hillsboro, OR, Purchased in Spain). The observations were conducted at 300 kV with 0.2 nm point resolution. The micrograph analysis, lattice spacing, fast Fourier transform (FFT), and the phase interpretation were performed with the Gatan Digital Micrograph® software (Gatan Inc., Pleasanton, CA, USA. Purchased in Spain). The powder samples were dispersed in acetone, and droplets of the suspension were deposited onto a carbon film grid.

3. Results and Discussion

3.1. Microstructural Charactrization

Figure 2 shows the XRD pattern for the as-milled powders, as a function of the milling time and device employed. The powders that were milled for 6 h with the vibratory 8000D mixer/mill® (SP10_6h), exhibited only the diffraction peaks of the corresponding raw powders, as follows: Ti (hcp structure and P63/mmc of SGS, COD ID no. 9008517), Nb (bcc structure and Im3m of SGS, COD ID No. 1539041), and Mn (bcc structure and I-43m of SGS, COD ID No. 9011068). This result indicates a negligible level of alloying at this stage of the milling process. In contrast, under the same milling conditions, powders that were milled in the planetary mill (PL10_6h) showed diffraction peaks that do not correspond to the raw materials (Ti, Nb, and Mn), and that could be assigned to face cubic-centered (Fm3m of SGS) and body cubic-centered (Im3m of SGS) phases. These phases are presumably fcc and bcc TiNbMn alloys, according to the literature for specimens with similar compositions [11]. Clearly, most of the peaks were partially unresolved, due to the peak widening; this effect can be attributable to the reduction in the crystalline domain size, as was subsequently corroborated.

The fcc and bcc phases were also indexed when the BPR was increased from 10 to 20 for the corresponding specimen that was milled for 6 h in the PM400 planetary ball mill (PL20_6h). No diffraction peaks for the elemental Ti, Nb, and Ta were detected, which suggests a total alloying. Additionally, a slight signal assigned to elemental Fe (ref. pattern no. 006–0696 in the COD), with a body cubic-centered structure (bcc and Im3m of SGS), was observed in this XRD pattern. This element was produced by the contamination from the stainless-steel milling media. However, this signal is practically negligible, which suggests a small amount of Fe at 6 h of milling time.

At 12 h of milling time (Figure 2b), the specimens that were milled using a BPR of 10 in each mill device (i.e., specimens SP10_12h and PL10_12h), showed similar XRD patterns to the specimen that was milled in the planetary mill at 6 h, with a BPR of 20 (PL20_6h). The fcc and bcc phases were detected with total absence of the diffraction peaks of the corresponding raw materials. The Fe contamination was also noticeable. When

the BPR was increased (PL20_12h), the XRD pattern showed a unique fcc alloy, obviously with the elemental Ti, Nb, and Mn raw materials. No bcc phase was detected, and the peak intensity for the Fe contamination increased in comparison with the PL10_12h and SP10_12h specimens. This last outcome is a direct consequence of the higher-energy milling process that produces higher-energy collisions and friction between the milling media and powders. The milling energy increased with the number of balls, as many ball-to-ball and ball-to-wall collisions occur, which lead to a greater increase in the average temperature of the milling media. Takacs et al. [22] proposed that the heating of the milling balls was due to the oblique collisions, and reported an average temperature of the milling balls in excess of 200 °C for the planetary ball mill, and below 100 °C for a shaker ball mill, both run under typical operating conditions. Moreover, Shelekhov et al. [23] predicted an increase in the planetary ball mill temperatures of up to 500 °C by computer simulation.

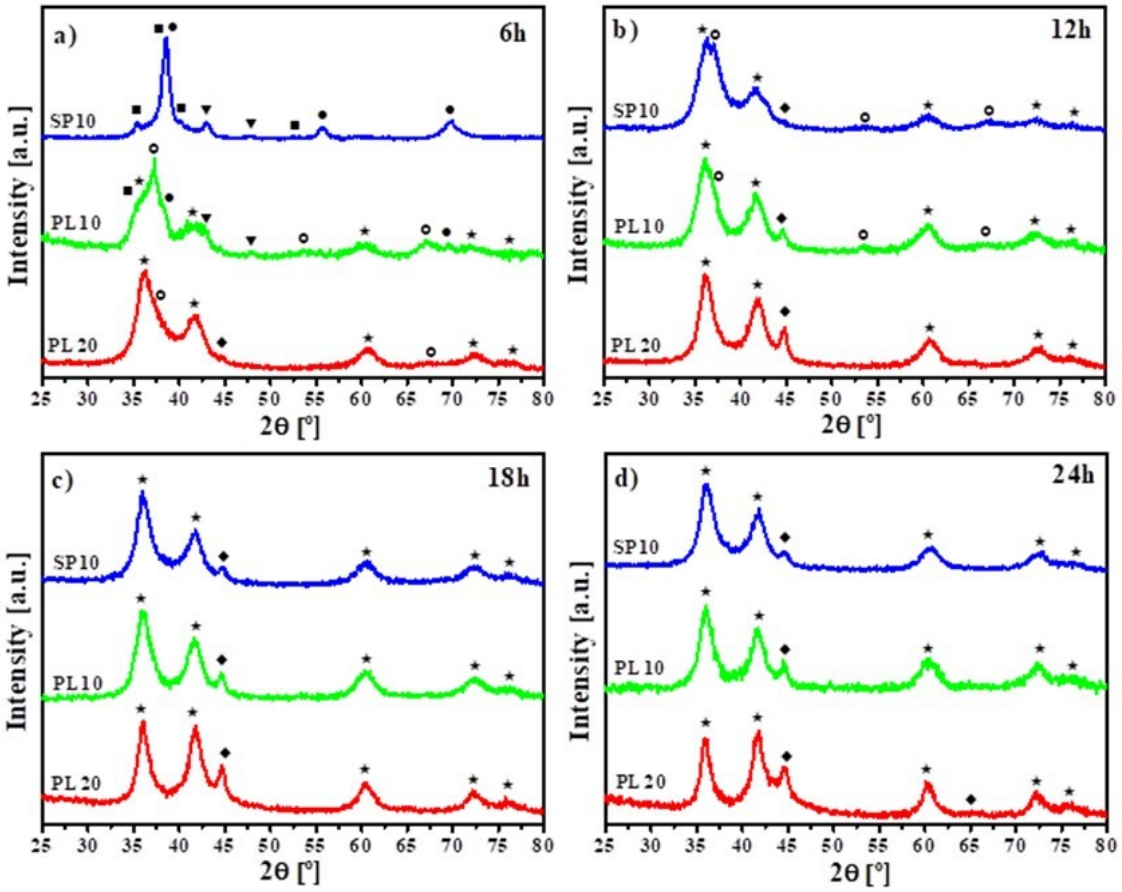

Figure 2. XRD patterns for the TiNb15Mn as-milled powdered mixtures, at 6 h (**a**), 12 h (**b**), 18 h (**c**) and 24 h (**d**). SP10: milled in the 8000D mixer/mill® with a BPR equal to 10; PL10 and PL20: milled in the PM 400 planetary mill with a BPR equal to 10 and 20, respectively. (■) Ti (hcp, P63/mmc SGS); (●) Nb (bcc, Im3m SGS); (▼) Mn (bcc, I-43m SGS); (○) bcc-TiNbMn alloy (Im3m SGS); (★) fcc-TiNbMn alloy (Fm3m SGS); (♦) Fe (bcc, Im3m SGS).

When the milling time was extended to 18 h (Figure 2c) and 24 h (Figure 2d), all the specimens showed similar XRD patterns, and the fcc phase was reported with no presence of the bcc phase. This suggested that the final fcc phase is the stable phase in this TiNb15Mn system. This final stable phase seems to be achieved after 12 h of milling time for the PL20 specimen, or after 18 h for the SP10 and PL10 specimens. Therefore, the time required to reach the full transformation of raw powders to the fcc phase is relatively short in comparison with similar studies on Ti fcc phase formation, such as the Ti–Ta–Sn system (Ti–13Ta–6Sn [24]), and the Ti–Nb–Ta–Mn system (Ti–30Nb–13Ta–2Mn [13]), where milling times between 50–100 h were necessary. The corresponding peak to the Fe contamination

presented in all of the specimens that were milled for 18 h and 24 h, showed an increasing intensity for both the milling times, according to the following sequence: SP10 → PL10 → PL20. However, the (110) Fe peak position remains invariant (2θ = 44.7°), which suggests unalloyed Fe. This aspect can be attributed to the negligible solubility between Fe–Ti and Fe–Nb at temperatures below 700 °C [25,26], according to the binary phase diagrams. Moreover, this temperature was avoided in the milling process, due to the start/stop procedure that was employed. In addition, the Fe particles were continuously incorporated into the milling, by the chipping of the milling media, and the macroscopic Fe particles are later crushed to form isolated microparticles. Therefore, the particles could be found in various sizes, as will be later corroborated by XEDS-SEM analysis and remain unalloyed throughout the milling, according to the XRD measurement.

Subsequently, since the DRX patterns of Figure 2 showed many unresolved diffraction peaks between 2θ = 30°–50°, a deconvolution process was carried out to corroborate the phase indexation performed (Figures 3 and 4). The goodness-of-fit for the deconvolution processes was determined by the chi-square (χ^2) parameter, which is the typical parameter used for Rietveld analysis [27]. This parameter, usually close to one, was determined in all the cases to be approximately 1.4, thereby verifying the quality of the goodness-of-fit. The peak deconvolution process was therefore made for the specimens that were alloyed in the 8000D mixer/mill® (Figure 3), between 6 h and 24 h of milling time (i.e., SP10_6h, SP10_12h, SP10_18h, and SP10_24h). At the lowest milling time, SP10_6h (Figure 3a), the deconvoluted peaks matched the peaks of the raw transition metals (Ti, Nb, and Mn) that were previously indexed in Figure 2. However, an optimal deconvolution fitting was reached when a small reflection was added. Due to the low intensity, this reflection may be the bcc phase in an early state. At 12 h of milling time, SP10_12h (Figure 3b), the alloying process was complete, due to the coexistence of the bcc and fcc phases. For the two highest milling times, SP10_18h (Figure 3c) and SP10_24h (Figure 3d), the deconvolution process showed compelling results. In this case, the bcc phase was detected, although it could not be observed in Figure 2. The diffraction peak of the bcc phase became narrower and lower in intensity with the increase in milling time, while the peak intensity of the fcc phase increased. Therefore, the full conversion from raw materials to a unique fcc alloy was not totally reached after 24 h of milling time using the 8000D mixer/mill® (Figure 3d).

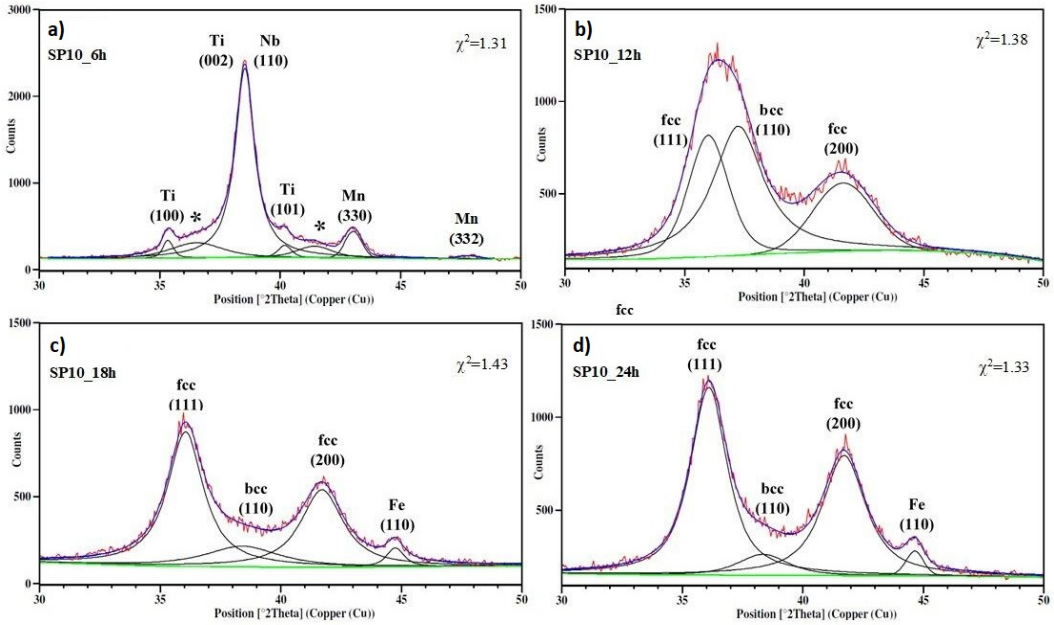

Figure 3. Deconvoluted XRD patterns in the 30°–50° 2θ range, for the SP10 specimens milled at 6 h (**a**), 12 h (**b**), 18 h (**c**), and 24 h (**d**). The reflections for elemental Ti, Nb, Mn, Fe (this last from contamination), the bcc-, and the fcc-TiNbMn alloys. In brackets are marked the (hkl) Miller index for the corresponding reflections; * unindexed slight peak.

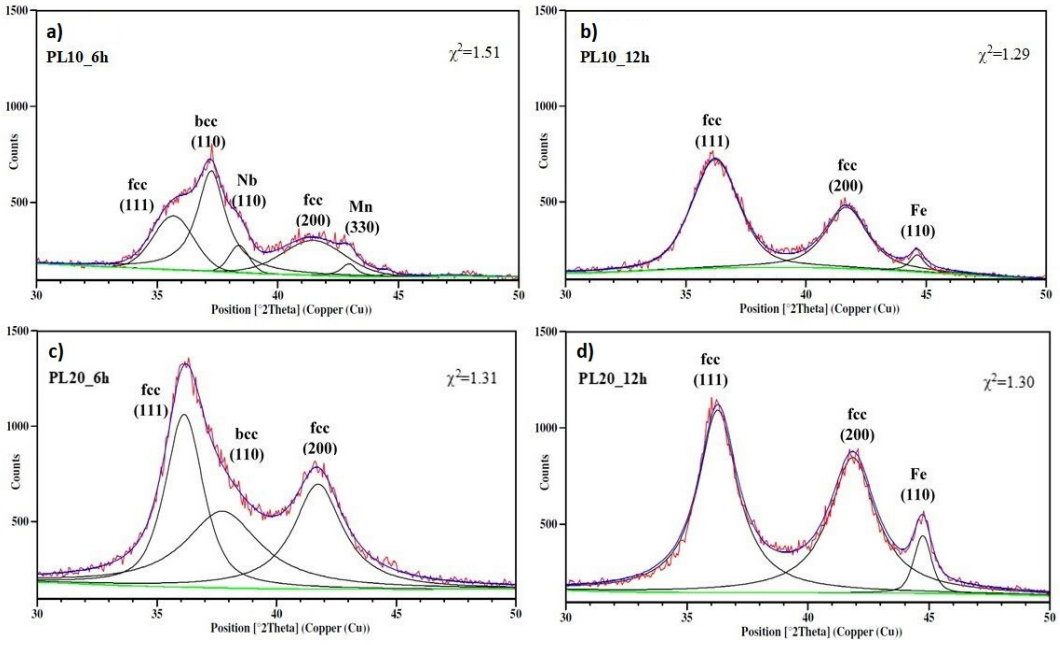

Figure 4. Deconvoluted XRD patterns in the 30°–50° 2θ range, for the PL10_6h (**a**), PL10_12h (**b**), PL20_6h (**c**) and PL20_12h (**d**) specimens. It is showed the reflections for elemental Nb, Mn, Fe (this last from contamination), the bcc-, and the fcc-TiNbMn alloys. In brackets are marked the (hkl) miller index for the corresponding reflections.

The same XRD deconvolution process was carried out for specimens that were alloyed in the planetary mill for 6 h (Figure 4a) and 12 h (Figure 4b). In this case, the deconvolution peaks were in good agreement with the results shown in the general XRD diffraction patterns (Figure 2). Therefore, the full conversion of the fcc phase from Ti, Nb, and Mn raw materials without the bcc phase, was reached after 12 h of milling time, using a BPR of 10 (PL10_12h) or 20 (PL20_12h).

According to the XRD results obtained in this work, the following alloying route could be proposed: raw elements (Ti, Nb, Mn) → bcc phase → (bcc + fcc) phases → fcc phase.

This route could be explained as being due to the allotropic transformation of the TiNbMn alloy from a bcc to fcc crystallographic structure. Although this allotropic transformation is not common in beta-stabilized Ti alloys (bcc-Ti alloys), it has been previously reported in systems with Nb as a main alloying element, such as the Ti–30Nb–13Ta–2Mn alloy, Ti–Nb–Ta system, and TiNb*x*Mn (x = 0–12 wt.%), among others [8,9,11,13,24]. This transformation is directly associated with the combination of the Nb content and mechanical milling, as first reported by Chattopadhyay et al. [28].

Table 1 showed the crystalline domain size D, determined for both the bcc and fcc phases, using the deconvolved peaks and the Scherrer formula. As a general trend, a nanodomain character could be determined for both the mills and BPR. All the specimens showed D values between 1.7 to 4.7 nm, approximately.

For the bcc phase, a slight reduction in D was observed with the milling time, for the specimens that were milled in the 8000D mixer/mill® (SP10_12h, SP10_18h, and SP10_24h), from 1.7 to 3.1 nm. This behavior could enhance the diffusion of the elements between the bcc and fcc phases, thereby contributing positively to the allotropic transformation of the TiNbMn alloy, thanks to the reduction in the diffusion path in the volume of the grain, and also thanks to the increase in the grain boundaries (diffusion-induced grain migration (DIGM)) [29]. At the same time, the D values of the bcc phase in the specimens that were alloyed in the planetary mill were only determined at 6 h of milling time, since the bcc phase became a transitory phase that is totally transformed into the fcc phase at 12 h. Thus, due to the higher energy that was transferred to the powders when BPR = 20 was used in comparison with BPR = 10, the D value for the bcc phase for PL20_6h was lower than the PL10_6h (2.3 nm and 4.4 nm, respectively).

Table 1. Crystalline domain size (D) and lattice parameters (a = b = c) for both bcc-TiNb15Mn and fcc-TiNbMn alloys synthesized in all as-milled powders. ND = phase not detected.

	D (nm)				a (Å)			
	bcc-TiNb15Mn							
	6 h	**12 h**	**18 h**	**24 h**	**6 h**	**12 h**	**18 h**	**24 h**
SP10	ND	3.1	2.5	1.7	ND	3.4139	3.3179	3.3145
PL10	4.4	ND	ND	ND	3.4139	ND	ND	ND
PL20	2.3	ND	ND	ND	3.3718	ND	ND	ND
	fcc-TiNb15Mn							
	6 h	**12 h**	**18 h**	**24 h**	**6 h**	**12 h**	**18 h**	**24 h**
SP10	ND	3.8	3.4	3.6	ND	4.3310	4.3314	4.3326
PL10	4.0	3.0	3.0	3.5	4.3336	4.3330	4.3335	4.3348
PL20	3.4	3.0	4.0	4.7	4.3284	4.3292	4.3290	4.3316

On the other hand, the D value for the fcc phase remained practically invariant when this phase coexisted with the β phase, probably since the transferred energy was largely employed to enhance the diffusion of elements, instead of to increase the plastic deformation of particles and diminish the D value. When only the fcc phase was present, the D value increased with the milling time, from 3.0 to 3.5 nm for PL10, and from 3.0 to 4.7 nm for PL20; the reason for this being that during the transformation from the bcc phase to the fcc phase, most of mechanical energy was used for this purpose. However, when the fcc phase was completely formed, the energy that was transferred from the mill to the powders was utilized to increase the D value. This effect was more pronounced for higher energetic milling conditions (PL20 specimens).

The lattice parameter a for the fcc and bcc phases was also determined from the refined position of the deconvolved peaks (Table 1). In this case, the corresponding lattice parameters for the bcc transition phase were higher than those corresponding to elemental Nb (a = 3.303 Å, in COD ID no. 1539041), for lower milling times, but when the milling time was increased for the SP10 specimens (SP10_12h, SP10_18h, and SP10_24h), the lattice parameter was reduced to values close to those of the elemental Nb. This aspect suggests the introduction of Ti and/or Mn atoms into the Nb crystal structure first at a lower milling time, and the subsequent promotion of the diffusion of Ti and Mn alloying elements from the bcc phase to the fcc phase at higher milling times.

Furthermore, the lattice parameters for the fcc phase remained practically invariant, regardless of the milling process (i.e., SP10, PL10, and PL20). This result suggests an optimal homogenization of the Ti, Nb, and Mn atoms within the fcc phase, even when the milling time was increased. The difference in the y-axis amplitude for both b (from 3.30 Å to 3.50 Å, i.e., 0.2 Å of amplitude) and g (from 4.32 Å to 4.35 Å, i.e., 0.03 Å of amplitude) corroborates the higher homogenization of the final fcc phase.

Finally, it should be borne in mind that the Fe lattice parameters that were obtained for all the specimens from the milling media, were close to those corresponding to the elemental Fe (2.867 ± 0.02 Å from XRD vs. 2.866 Å from ref. pattern no. 006–0696 in the COD). This aspect, together with the absence of any intermetallic compounds, suggests that the Fe is mostly unalloyed in the specimens that were obtained.

3.2. Morphology and Compositional Characterization

The particle morphology and average-size characterization of the synthesized phases were carried out using SEM images of the specimens after 6 h of milling time (Figure 5). The SP10_6h powders, Figure 5a,b, presented the characteristic morphology features of an early stage of a mechanical alloying process [17], such as the following: (a) coarsened particles, due to plastic deformation and the cold welding of fine particles to coarse particles (marked with square dots in Figure 5b); and (b) a powder size reduction, due to multiple particle

fractures (marked with white arrow dots in Figure 5b). These features are characteristic of ductile powders in the early stages of the milling process, due to repeated impacts between the balls and particles [17]. During MA, the powder particles are repeatedly flattened, cold-welded, fractured, and re-welded. The cold welding and fracturing processes can be predominant at any stage, and depends mainly on the deformation characteristic of the raw powders.

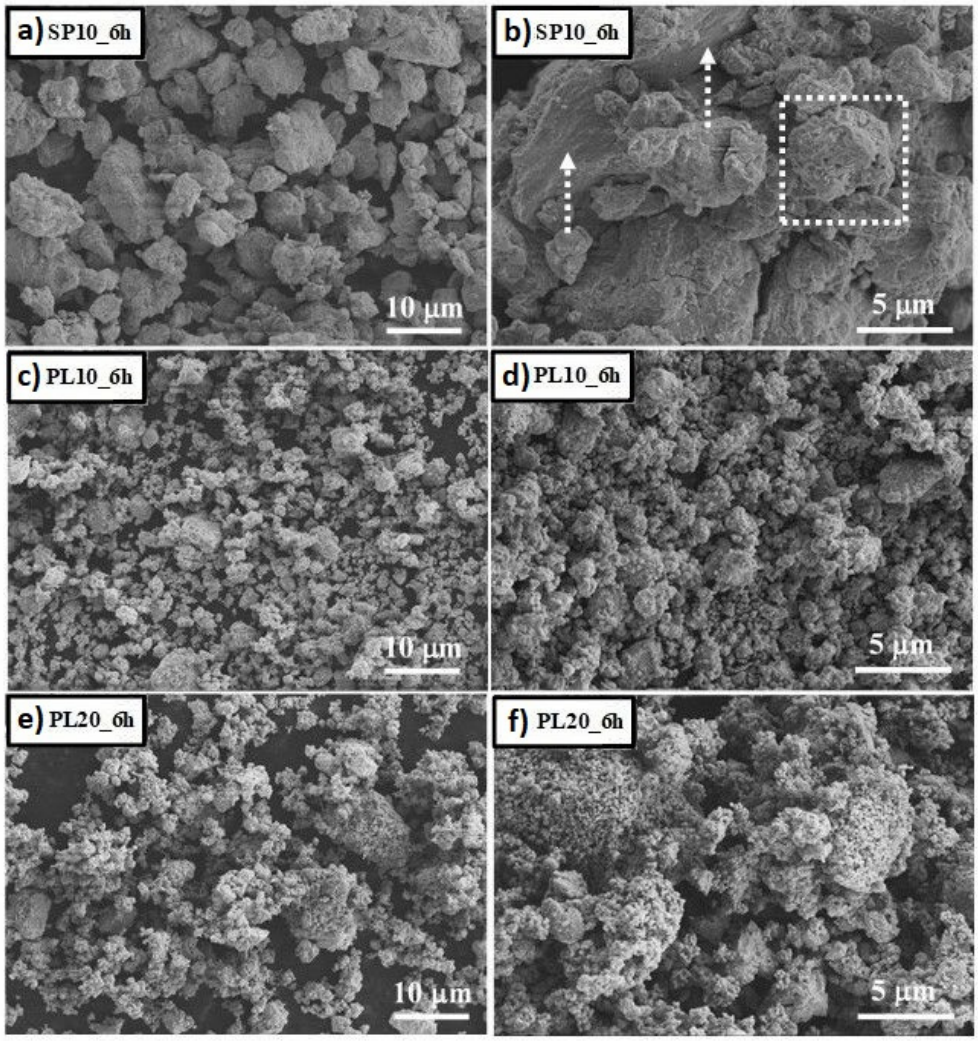

Figure 5. Scanning electron microscopy (SEM) images for the TiNb15Mn alloy milled at 6 h and for both 8000D mixer/mill® and PM400 devices and at BPR equal to 10 and 20, i.e., SP10_6h (**a**,**b**), PL10_6h (**c**,**d**) and PL20_6h (**e**,**f**). Cold-welded particles are marked with dotted squares, and the typical fractured particles are marked by dotted arrows.

The SEM images of the PL10_6h particles (Figure 5c,d) and PL20_6h particles (Figure 5e,f) showed smaller and irregular particles with a high level of agglomeration, which is a clear indication of an advanced state of the milling and alloying process. As the MA continues, the energy transferred from the balls to the powder produced large grain boundary surface areas (reduced grain size), and the crystal defect density increased. These new surfaces enabled the particles to weld together much more easily, thereby leading to an increase in the particle agglomeration. Furthermore, at higher BPR (PL20_6h), the particles exhibited a spherical shape, due to the reduction in the Gibbs free energy during the milling process. The average particle size was estimated at 8.1 ± 3 µm, 3.3 ± 1.6 µm, and 0.8 ± 0.3 µm, for SP10_6h, PL10_6h, and PL20_6h, respectively. Clearly, the particle size was further reduced when the milling energy that was employed was increased. The parti-

cles at PL20_6h showed a significant level of agglomeration, due to their submicrometric size range.

To corroborate the chemical composition of the bcc and fcc phases as two TiNbMn alloys, together with the distribution of Ti, Nb, and Mn across the different particles, XEDS-SEM maps were used and average compositional analysis by XEDS was carried out over the specimens that were milled in the 8000D mixer/mill® (SP10_6h, SP10_12h, and SP10_18h, Figure 6) and the PM400 planetary ball mill (PL10_6h and PL10_12h, Figure 7).

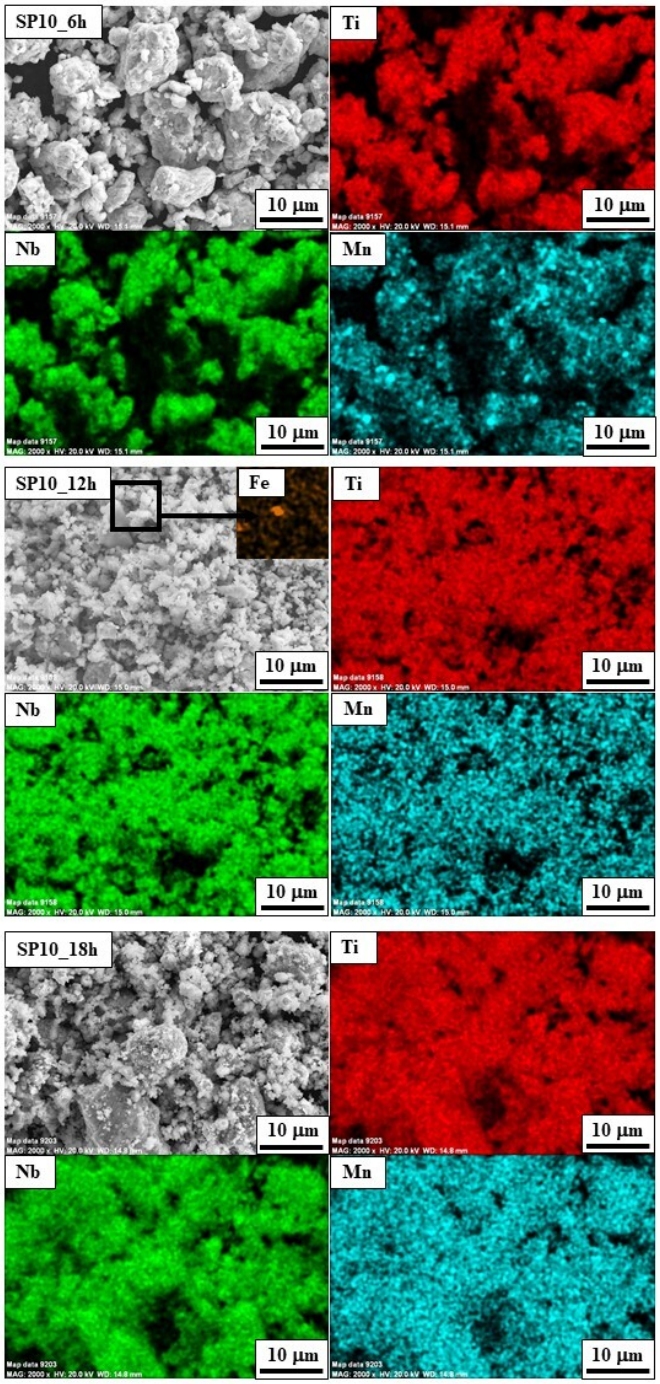

Figure 6. Characteristic compositional XEDS-SEM mapping for the elements existing in the SP10 specimens milled at 6 h, 12 h, and 18 h. Ti: red; Nb: green; Mn: light blue; Fe: orange.

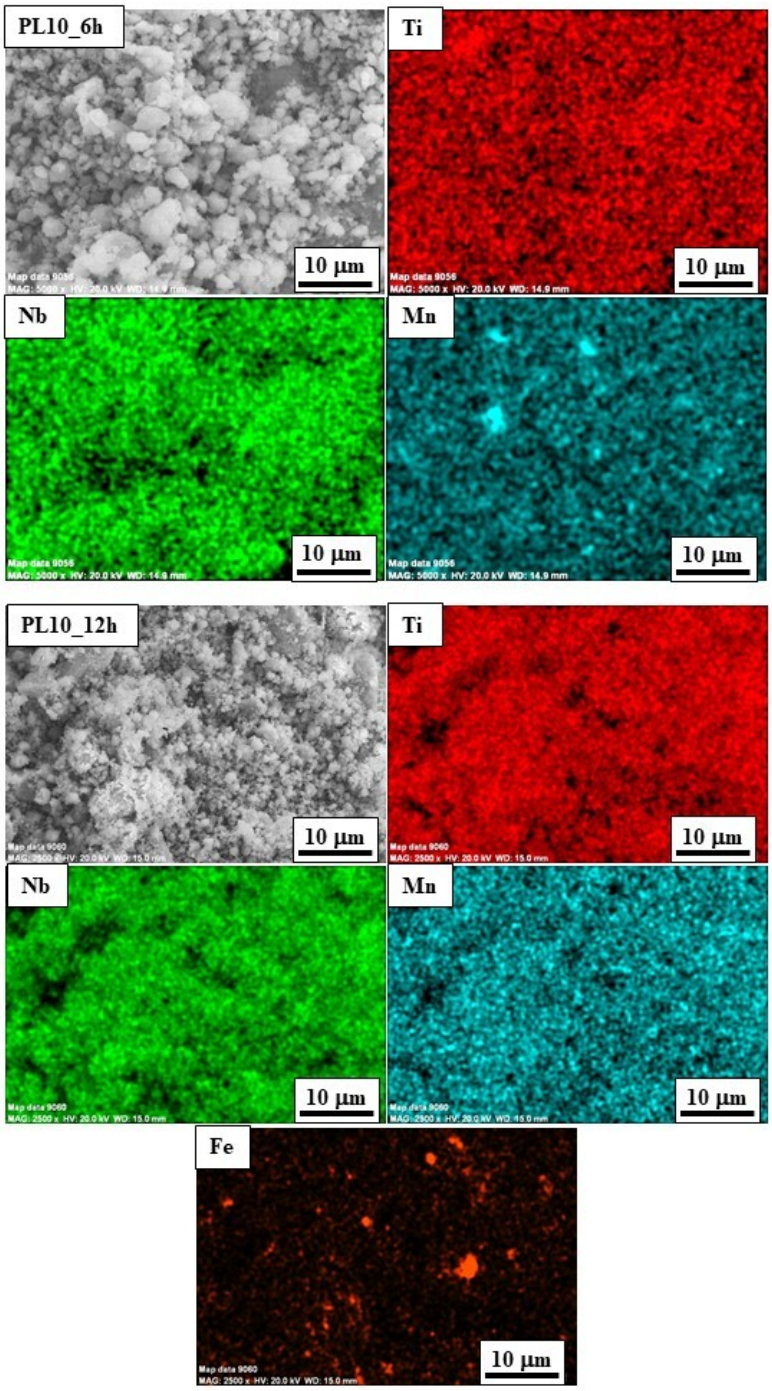

Figure 7. Characteristic compositional XEDS-SEM mapping for the elements existing in the PL10 specimens milled at 6 h and 12 h. Ti: red; Nb: green; Mn: light blue; Fe: orange.

After 6 h of milling time, the Ti and Nb elements in the SP10_6h seemed to be highly alloyed, due to the uniform contrast that was observed across all the particles in the corresponding Ti (red color) and Nb (green color) XEDS-SEM micrographs, although the Mn (light-blue color) was unevenly distributed across the particles. These results are in good agreement with the deconvoluted XRD patterns that are shown in Figure 3a, where a low intense Ti (100) peak and a well-defined Mn peak were detected, corroborating the not total conversion of Ti, and mainly Mn, into the TiNbMn alloy. The difference between the degrees of alloying could be associated with the higher solubility of Ti and Nb than Mn, as can be corroborated by the corresponding Ti–Nb and Mn–Nb phase diagrams [30–32].

Subsequently, at 12 h and 18 h (SP10_12h and SP10_18h) of milling time, the element distribution that was observed for Ti, Nb, and Mn in the XEDS maps across the different particles, seems to be uniform, which suggests a similar composition in all the particles. This result is significant, due to the major fcc phase and minor bcc phase that were detected in the deconvoluted XRD patterns (Figure 3), where both the phases are expected to present similar composition. Thus, the relative Ti–Nb–Mn stoichiometry, determined by EDS using 20 points, yielded $Ti_{0.57\pm0.02}Nb_{0.27\pm0.02}Mn_{0.16\pm0.01}$ for SP10_12h and $Ti_{0.56\pm0.02}Nb_{0.28\pm0.02}Mn_{0.16\pm0.02}$ for SP10_18h. The low standard deviation obtained helps to corroborate the similar composition of the bcc and fcc phases, which are, in fact, two TiNb15Mn alloys. Furthermore, few Fe particles could be detected in the SP10_12h specimen and SP10_18h specimens. By general EDS measurements, these specimens showed a total Fe amount of 1.3 ± 0.2 wt.% and 3.6 ± 1.2 wt.%, respectively.

A similar evolution was observed according to the XEDS-SEM maps for the specimens that were milled in the planetary mill under similar conditions, that is, the PL10 specimens (Figure 7). After 6 h of milling time, PL10_6h, the Ti was uniformly distributed across all the particles, while the Mn showed an uneven distribution. These results corroborate the effortless alloying process of Ti with Nb, which contrast with the Mn–Nb system. Therefore, the atomic diffusion that is necessary to produce the alloying process is mainly controlled by thermodynamic aspects, which are fully achievable with the energy transferred by both the 8000D mixer/mill® and the PM400 Retsch® planetary ball mill. At 12 h of milling time, PL10_12h, the specimens showed a clear uniform distribution of the three Ti, Nb, and Mn elements, thereby indicating the formation of a single TiNb15Mn alloy, with an fcc crystal structure, as revealed by the deconvoluted XRD pattern (Figure 4). The stoichiometry composition that was obtained for the fcc-TiNbMn phase was as follows: $Ti_{0.55\pm0.02}Nb_{0.28\pm0.01}Mn_{0.16\pm0.01}$, which was similar to that obtained by the 8000D mixer/mill®. On the other hand, a significant amount of unalloyed Fe was detected (3.1 ± 0.5 wt.%). Finally, it is important to note that the maximum Fe amount was found for the specimen SP20_24h (12.1 ± 1.1 wt.%). In this context, a 12.1 wt.% of Fe in this SP20_24h is inadmissible, disabling the specimens milling in the planetary mill during 24 h at with a BPR equal to 20 for potential applications, such as the bone-replacement implant materials abovementioned.

Finally, a crystallographic study was carried out by HRTEM, ED, and FFT in the SP10_18h (Figure 8) and PL10_24h (Figure 9) specimens, to corroborate the phase identification for the synthesized TiNb15Mn alloy. For the SP10_18h specimen, the milled powders exhibited a submicrometric particle size of approximately 0.2–0.3 microns (Figure 8a). The HRTEM (Figure 8b) and FFT (Figure 8c) images that were obtained in a selected particle show the concentric diffraction rings corresponding to the fcc-TiNb15Mn alloy. The crystallographic planes of the fcc phase, (111), (200), and (220), indicated in Figure 8c, are in good agreement with the corresponding interplanar distances determined by XRD, as shown in Table 2. Two opposing points (marked with red circles in Figure 8c) were detected between the rings corresponding to the (111) and (200) crystallographic planes. These points could correspond to the (110) crystallographic plane for the bcc-TiNb15Mn alloy. The bcc phase had already been detected in the deconvoluted XRD diffractogram pattern (Figure 3), where only a small single domain could be ascertained, but here, the interplanar distance and lattice parameter calculated for this (110) crystallographic plane are in concordance with the value obtained by XRD (Table 1). Furthermore, the HRTEM (Figure 8d) and FFT (Figure 8c) images that were obtained in a different particle, show a diffuse amorphous halo, which could be attributed to a partial amorphization process, induced by the mechanical alloying. According to Aguilar et al. [33], the reduction in the Gibbs amorphization energy is enhanced by the addition of Mn to Ti.

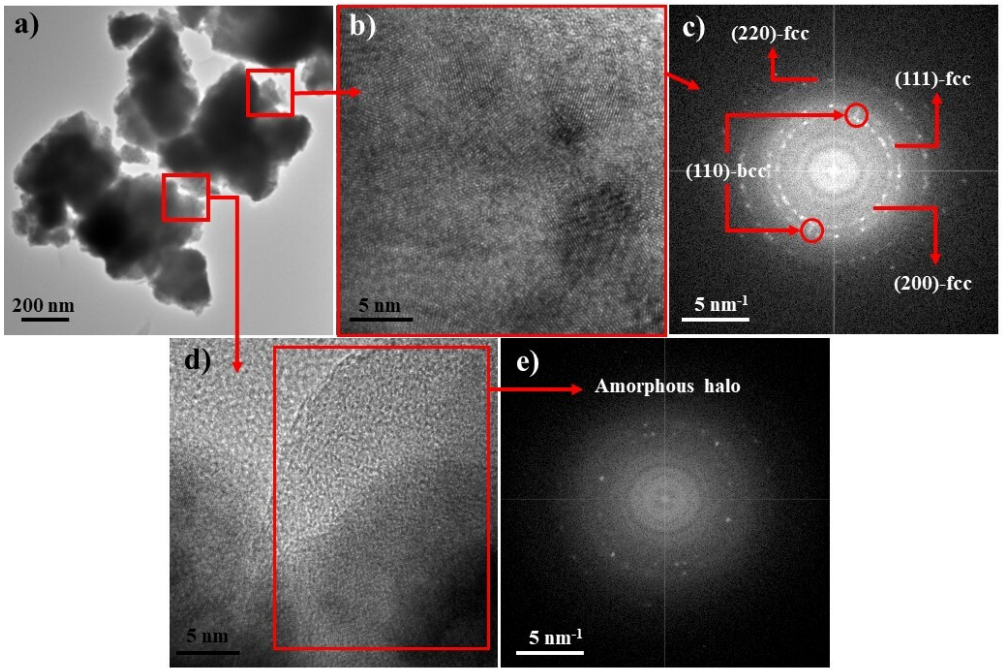

Figure 8. Transmission electron microscopy (TEM) study for theTiNb15Mn alloy milled after 18 h in the 8000D mixer/mill® (SP10_18h). (**a**) TEM image; (**b**,**d**) high-resolution TEM images; (**c**,**e**) the corresponding FFT images.

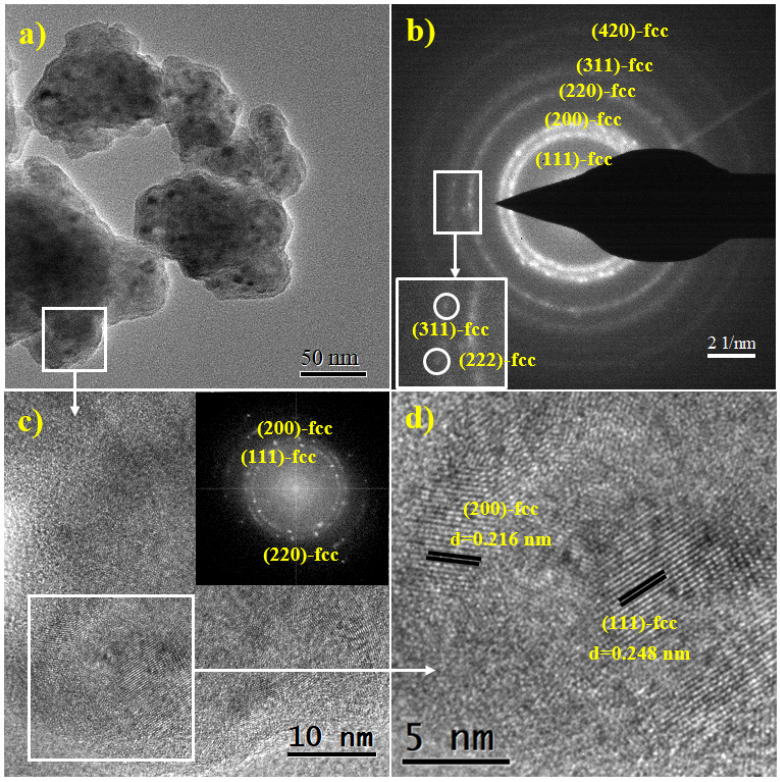

Figure 9. Transmission electron microscopy (TEM) study for the TiNb15Mn alloy milled after 24 h in the 8000D mixer/mill® (SP10_24h). (**a**) TEM image; (**b**) electron diffraction (ED) image; (**c**) and (**d**) high-resolution TEM images; inset in (**c**) the corresponding FFT image.

Table 2. Interplanar distances and the corresponding lattice parameters (a) determined by HRTEM-FFT for both bcc-TiNb15Mn and fcc-TiNbMn alloys in the SP10_18h and SP10_24h specimens. ND = crystallographic plane not detected; CP = crystallographic plane.

CP	fcc-TiNbMn		CP	bcc-TiNb15Mn
	SP10_18h	SP_24h		SP10_18h
(111)	0.2510	0.2491	(110)	0.2345
(200)	0.2161	0.2171	a (nm)	0.3316
(220)	0.1533	0.1532	-	-
(311)	ND	0.1301	-	-
(222)	ND	0.1255	-	-
(400)	ND	0.1092	-	-
a (nm)	0.4328 ± 0.001	0.4325 ± 0.011	-	-

The PL10_24h specimen (Figure 9a) showed powder with a nanometric particle size of approximately 100 nm, as expected from the increased milling time and energy delivered by the PM400 Retsch® planetary mill. The direct ED patterns that were obtained from Figure 9a only show concentric rings corresponding to the fcc-TiNb15Mn alloy (Figure 9b), which is in concordance with the XRD results in Figure 2. The observed crystallographic planes were indicated on the image (Figure 9b), and the corresponding interplanar distances were described in Table 2. Finally, the following two different aspects deserve to be highlighted in comparison with the SP10_18h TEM study: (1) in this specimen, no indication of the bcc-TiNb15Mn phase was found, which corroborated the complete allotropic transformation of the alloy from bcc to fcc; and (2) no amorphous phase was detected, most probably due to the higher energy transferred from the planetary mill in comparison with that from the 8000D mixer/mill®.

4. Conclusions

A ternary TiNb15Mn alloy, with nominal compositions of 42.5 wt.% of Ti, 42.5 wt.% of Nb, and 15 wt.% of Mn, was successfully synthesized by two different high-energy milling devices (8000D mixer/mill® and PM400 planetary ball mill), and by two different ball-to-powder ratios (BPR), 10 and 20. The ternary TiNb15Mn alloy showed an unusual fcc structure for a Ti alloy (fcc-Ti alloy), instead of the usual hcp-Ti alloy or bcc-Ti alloy, caused by the allotropic transformation of the bcc-Nb alloy during mechanical milling. This synthesis evolved, as a general trend, and in all mechanical alloying conditions, from the raw materials (Ti, Nb, and Mn) to an intermediate bcc-TiNb15Mn alloy, and, finally, to the fcc-TiNb15Mn alloy. The full conversion to the final fcc-TiNb15Mn alloy was only reached in the planetary mill at a BPR equal to 10 and 20, and from 12 h of milling time, that is, the PL10_12h and PL20_12h specimens. For the 8000D mixer/mill®, due to the lower energy transferred from the milling media to the mixture of powders, a remnant unconverted bcc-TiNb15Mn alloy was detected. In all the cases, the synthesized fcc-TiNb15Mn alloy presented a nanocrystalline nature and partial amorphization. On the other hand, the specimen that was milled in the planetary mill after 24 h and BPR 20 (PL20_24h), showed a significant amount of Fe contamination from the milling media (12.1 wt.%), disabling its use for future applications. Finally, to decrease the full conversion time, a planetary mill should be used for a mechanical alloying process, while, to diminish the contamination, an 8000D mixer/mill® would provide the most suitable option.

Author Contributions: Conceptualization, C.G.-G., R.S.F. and E.C.; methodology, C.G.-G. and E.C.; formal analysis, C.G.-G., C.S. and L.P.-P.; investigation, C.G.-G., C.S., L.G.-D., P.J.L.-J., L.P.-P. and E.C.; resources, R.S.F., E.C.; writing—original draft preparation, C.G.-G., C.S., L.G.-D. and P.J.L.-J.; writing—review and editing, C.G.-G., R.S.F., L.P.-P. and E.C.; visualization, C.G.-G., P.J.L.-J. and L.P.-P.; supervision, E.C.; project administration, E.C.; funding acquisition, E.C. All authors have read and agreed to the published version of the manuscript.

Funding: This research was funded by the FONDECYT fund (Government of Chile), grant no. 3150060. The characterization studies were financed under project No. 2021/00000691 by the VI Research Program of the University of Seville.

Institutional Review Board Statement: Not applicable.

Informed Consent Statement: Not applicable.

Data Availability Statement: Not applicable.

Acknowledgments: P.J., Lloreda-Jurado would like thanks to the University of Seville for his financial support (grant PIF II.2A, through VI Plan Propio de Investigación).

Conflicts of Interest: The authors declare no conflict of interest. The funders had no role in the design of the study; in the collection, analyses, or interpretation of data; in the writing of the manuscript, or in the decision to publish the results.

References

1. Peters, M.; Leyens, C. Fabrication of Titanium Alloys. In *Titanium and Titanium Alloys: Fundamentals and Applications*, 1st ed.; Wiley-VCH Verlag GmbH & Co. KGaA: Weinheim, Germany, 2003; pp. 393–497. [CrossRef]
2. Peters, M.; Hemptenmacher, J.; Kumpfert, J.; Leyens, C. Structure and Properties of Titanium and Titanium Alloys. In *Titanium and Titanium Alloys*, 1st ed.; Peters, M., Leyens, C., Eds.; Wiley-VCH Verlag GmbH & Co. KGaA: Weinheim, Germany, 2005; pp. 1–36.
3. Geetha, M.; Singh, A.K.; Asokamani, R.; Gogia, A.K. Ti based biomaterials, the ultimate choice for orthopaedic implants—A review. *Prog. Mater. Sci.* **2009**, *54*, 397–425. [CrossRef]
4. Davies, P.; Johal, A.; Davies, H.; Marchisio, S. The fatigue performance of titanium alloys joined via the powder interlayer bonding method. *Int. J. Adv. Manuf. Syst.* **2020**, *109*, 1553–1561. [CrossRef]
5. Williams, J.C.; Boyer, R.R. Opportunities and issues in the application of titanium alloys for aerospace components. *Metals* **2020**, *10*, 705. [CrossRef]
6. James, S.; Kosaka, Y.; Thomas, R.; Garratt, P. Timetal® 407: A Titanium Alloy to Enable Cost Reduction. In Proceedings of the 13th World Conference on Titanium, San Diego, CA, USA, 16–20 August 2015; pp. 721–725. [CrossRef]
7. Kolli, R.P.; Devaraj, A. A review of metastable beta titanium alloys. *Metals* **2018**, *8*, 506. [CrossRef]
8. Chicardi, E.; Gutiérrez-González, C.F.; Sayagués, M.J.; García-Garrido, C. Development of a novel TiNbTa material potentially suitable for bone replacement implants. *Mater. Des.* **2018**, *145*, 88–96. [CrossRef]
9. García-Garrido, C.; Gutiérrez-González, C.; Torrecillas, R.; Pérez-Pozo, L.; Salvo, C.; Chicardi, E. Manufacturing optimisation of an original nanostructured (beta + gamma)-TiNbTa material. *J. Mater. Res. Technol.* **2019**, *8*, 2573–2585. [CrossRef]
10. Aguilar, C.; Martinez, C.; Tello, K.; Palma, S.; Delonca, A.; Martín, F.S.; Alfonso, I. Thermodynamic analysis of the formation of FCC and BCC solid solutions of ti-based ternary alloys by mechanical alloying. *Metals* **2020**, *10*, 510. [CrossRef]
11. Chicardi, E.; Aguilar, C.; Sayagués, M.J.; García-Garrido, C. Influence of the Mn content on the TiNbxMn alloys with a novel fcc structure. *J. Alloys Compd.* **2018**, *746*, 601–610. [CrossRef]
12. Santos, P.F.; Niinomi, M.; Liu, H.; Cho, K.; Nakai, M.; Itoh, Y.; Narushima, T.; Ikeda, M. Fabrication of low-cost beta-type Ti-Mn alloys for biomedical applications by metal injection molding process and their mechanical properties. *J. Mech. Behav. Biomed. Mater.* **2016**, *59*, 497–507. [CrossRef]
13. Salvo, C.; Aguilar, C.; Cardoso-Gil, R.; Medina, A.; Bejar, L.; Mangalaraja, R.V. Study on the microstructural evolution of Ti-Nb based alloy obtained by high-energy ball milling. *J. Alloys Compd.* **2017**, *720*, 254–263. [CrossRef]
14. Wu, H.C.; Kumar, A.; Wang, J.; Bi, F.; Tomé, C.N.; Zhang, Z.; Mao, S.X. Rolling-induced Face Centered Cubic Titanium in Hexagonal Close Packed Titanium at Room Temperature. *Sci. Rep.* **2016**, *6*, 24370. [CrossRef]
15. Hong, D.H.; Lee, T.W.; Lim, S.H.; Kim, W.Y.; Hwang, S.K. Stress-induced hexagonal close-packed to face-centered cubic phase transformation in commercial-purity titanium under cryogenic plane-strain compression. *Scr. Mater.* **2013**, *69*, 405–408. [CrossRef]
16. Normand, J.; Moriche, R.; García-Garrido, C.; Ferrer, R.E.S.; Chicardi, E. Development of a TiNbTaMoZr-based high entropy alloy with low young's modulus by mechanical alloying route. *Metals* **2020**, *10*, 1463. [CrossRef]
17. Suryanarayana, C. Mechanical alloying and milling. *Prog. Mater. Sci.* **2001**, *46*, 1–184. [CrossRef]
18. Takacs, L.; Šepelák, V. Quantitative comparison of the efficiency of mechanochemical reactors. *J. Mater. Sci.* **2004**, *39*, 5487–5489. [CrossRef]
19. De la Obra, A.G.; Gotor, F.J.; Chicardi, E. Effect of the impact energy on the chemical homogeneity of a (Ti,Ta,Nb)(C,N) solid solution obtained via a mechanically induced self-sustaining reaction. *J. Alloys Compd.* **2017**, *708*, 1008–1017. [CrossRef]
20. Chicardi, E.; Gotor, F.J.; Alcalá, M.D.; Córdoba, J.M. Influence of milling parameters on the solid-gas synthesis of TiCxN1−x by mechanically induced self-sustaining reaction. *Powder Technol.* **2017**, *319*, 12–18. [CrossRef]
21. Young, R.A.; Wiles, D.B. Profile shape functions in Rietveld refinements. *J. Appl. Crystallogr.* **1982**, *15*, 430–438. [CrossRef]
22. Takacs, L.; McHenry, J.S. Temperature of the milling balls in shaker and planetary mills. *J. Mater. Sci.* **2006**, *41*, 5246–5249. [CrossRef]

23. Shelekhov, E.V.; Tcherdyntsev, V.V.; Pustov, L.Y.; Kaloshkin, S.D.; Tomilin, I.A. Calculation of Energy Intensity and Temperature of Mechanoactivation Process in Planetary Ball Mill by Computer Simulation. In *Investigations and Applications of Severe Plastic Deformation*, 1st ed.; Lowe, T.C., Valiev, R.Z., Eds.; Springer: Berlin, Germany, 2000; Volume 80, pp. 139–145. [CrossRef]
24. Aguilar, C.; Pio, E.; Medina, A.; Mangalaraja, R.V.; Salvo, C.; Alfonso, I.; Guzman, D.; Bejar, L. Structural Study of Novel Nanocrystalline fcc Ti-Ta-Sn Alloy. *Metall. Mater. Trans. A* **2019**, *50*, 2061–2065. [CrossRef]
25. Murray, J.L. The Fe−Ti (Iron-Titanium) system. *Bull. Alloy Phase Diagr.* **1981**, *2*, 320–334. [CrossRef]
26. Vob, S.; Palm, M.; Stein, S.; Raabe, D. Phase equilibria in the Fe-Nb system. *J. Phase Equilib. Diffus.* **2011**, *32*, 97–104. [CrossRef]
27. Toby, B.H. R factors in Rietveld analysis: How good is good enough? *Powder Diffr.* **2006**, *21*, 67–70. [CrossRef]
28. Chattopadhyay, P.P.; Pabi, S.K.; Manna, I. A metastable allotropic transformation in Nb induced by planetary ball milling. *Mater. Sci. Eng. A* **2001**, *304–306*, 424–428. [CrossRef]
29. Shtremel, M.A. Participation of diffusion in the processes of mechanical alloying. *Met. Sci. Heat Treat.* **2002**, *44*, 324–327. [CrossRef]
30. Okamoto, H. Supplemental literature review of binary phase diagrams: Ag-Sn, Al-Pd, Ba-Gd, Ba-Pr, Cu-P, Dy-Ni, Ga-Mn, Gd-Sb, Gd-Zr, Ho-Te, Lu-Sb, and Mn-Nb. *J. Phase Equilib. Diffus.* **2014**, *35*, 105–116. [CrossRef]
31. Moffat, D.L.; Kattner, U.R. Stable and metastable Ti-Nb phase diagrams. *Metall. Trans. A* **1988**, *19*, 2389–2397. [CrossRef]
32. Murray, J.L. The Mn-Ti (Manganese-Titanium) system. *Bull. Alloy Phase Diagr.* **1981**, *2*, 334–343. [CrossRef]
33. Aguilar, C.; Guzman, P.; Lascano, S.; Parra, C.; Bejar, L.; Medina, A.; Guzman, D. Solid solution and amorphous phase in Ti–Nb–Ta–Mn systems synthesized by mechanical alloying. *J. Alloys Compd.* **2016**, *670*, 346–355. [CrossRef]